

W. B. Zimmerman · J. M. Rees · T. J. Craven

## Rheometry of non-Newtonian electrokinetic flow in a microchannel T-junction

Received: 5 January 2006 / Accepted: 20 March 2006 / Published online: 3 May 2006  
© Springer-Verlag 2006

**Abstract** Two-dimensional finite element simulations of electrokinetic flow in a microchannel T-junction of a fluid with a Carreau-type nonlinear viscosity are presented. The motion of the electrical double layer at the channel walls is approximated by velocity wall slip boundary conditions. The fluid experiences a range of shear rates as it turns the corner, and the flow field is shown to be sensitive to the non-Newtonian characteristics of the Carreau model. A one-to-one mapping between the Carreau parameters and the end wall pressure is demonstrated through statistical analysis of the pressure profile for a broad range of physical and operating parameters. Such a mapping allows the determination of the Carreau parameters of an unknown fluid if the end wall pressure profile is known; thus a highly efficient viscometric device may be constructed. A graphical technique to show that the inverse problem is well posed is shown, and a method for solving the inverse problem is presented. The challenges that must be overcome before a practical device can be constructed are discussed.

**Keywords** Rheometry · Non-Newtonian · Inverse problems · Electrokinetic flow

### 1 Introduction

The miniaturization of fluidic systems has given rise to many exciting applications in biotechnology and

biochemistry. Reliable construction of devices having features in the range from about 1  $\mu\text{m}$  to 1 mm has opened the way for more accurate, efficient and inexpensive chemical production, analysis and separation. Improved reaction control is possible with microfluidics compared to conventional macroscopic reactors. Advantages of miniaturization also include reduced analysis time, portability, requirement of minute amounts of chemical agent and potential for parallel analysis for increased throughput, which is advantageous for biochemical screening. We are working towards the fabrication of laboratories on chips where fluids are manipulated, transported and tested in volumes ranging from picoliters to microliters. At these micro scales, the surface to volume ratio for fluid flow passages is large and there is the prospect of precise control over mass transfer, heat transfer and chemical reaction. These properties have made micro-channel networks an attractive solution in a wide range of problematic situations.

At the micro scale, surface phenomena become prominent and a range of physical effects that are unimportant for flow at larger scales can be employed. One such effect is electroosmosis, inducing flow using the movement of the thin double layer of charged fluid present at a liquid–solid interface under application of an electric field. Electroosmotic flow (EOF) can be used in place of pressure differences to drive flows through micro channels. The advantages over pressure flow include precise flow control through applied potential differences at electrodes, fluid speed is largely independent of channel size, and a flat velocity profile in straight channel sections avoids mixing and rheological changes produced by lateral velocity variation that is characteristic of pressure flow. Also, charged species present in the bulk of the liquid (outside the double layer) will migrate due to the electric field, a process known as electrophoresis. Flows that are influenced by these electrical effects are referred to as electrokinetic flows.

To the authors' knowledge, there is little experimental data and theoretical analysis in the literature concerning

---

W. B. Zimmerman · T. J. Craven  
Department of Chemical and Process Engineering,  
University of Sheffield, Newcastle Street,  
Sheffield S1 3DJ, UK

J. M. Rees (✉)  
Department of Applied Mathematics,  
University of Sheffield,  
Hicks Building, Hounsfield Road,  
Sheffield S3 7RH, UK  
E-mail: j.rees@shef.ac.uk  
Tel.: +44-114-2223782  
Fax: +44-114-2223739

the electrokinetic flow of non-Newtonian fluids. Solutions of polymers in an ionic solvent readily meet this criterion however. Existing techniques for the analysis of non-Newtonian behavior are predominantly based on one-dimensional shear flows, where the stress experienced by the fluid can be expressed through a single shear parameter for the whole flow. Commercial devices such as viscometers work on this principle, and as such many experiments are required to build a picture of a fluid's shear response at different rates of shear. To date piezo electric devices have not been used in microrheometry for pressure sensing. However, micron resolution particle image velocimetry ( $\mu$ -PIV) has been used for the location of surfaces (Stone et al. 2002), the measurement of shear stresses (Pommer and Meinhart 2005) and for the measurement of flowrates. Piezo electric pressure sensors are cheap candidates to replace this functionality for online sensors. The purpose of this paper is to illustrate their potential utility in microrheometry.

This work demonstrates a potential design for an electrokinetic flow rheometer in a microchannel through the use of numerical simulations. By taking advantage of the unique characteristics of electrokinetic flow, we seek to develop a device capable of testing a range of viscous response in a single experiment. By inducing a flow which exhibits many shear rates, but remains organized by the imposed electric field, it is proposed that a great deal of information about the fluid's rheological properties may be determined. We build on preliminary studies by Zimmerman (2004), MacInnes (2002), Rees and Zimmerman (2005) and Zimmerman et al. (2004), and examine the rheometry of a Carreau fluid undergoing electrokinetic flow in a T-junction.

The geometry was selected in order to force a range of shear rates in the ordinarily plug flow profile of an electrokinetic flow that is dragged along by a Debye double layer motion along the boundary. The range of shear rates leads to a non-uniform acceleration of the flow as the fluid "turns the corner" and accelerates away from the stagnation point. This renders the pressure field along the end-wall of the T-junction sensitive to the constitutive properties of a non-Newtonian fluid. If a one-to-one relationship exists between the end-wall pressure profile and the parameters of the Carreau model, then knowledge of the end-wall pressure profile should directly lead to the determination of the Carreau parameters. Thus a highly efficient viscometric device may be constructed which is able to characterize the viscous response to shear rate in a single experiment. We select a four-parameter Carreau model for the nonlinear viscosity and perform two-dimensional finite element simulations of electrokinetically driven flow in the T-junction to test this hypothesis.

Potential applications for a micro rheometer are many and varied. As a component in a lab-on-a-chip network, a micro rheometer could supply fluid composition data at strategic points in a chemical process. Real-time data from such a device could easily be used

by the process control system, allowing the dynamic alteration of control parameters, chemical concentrations, flow rates, etc. Many biological fluids of interest, for example protein chains in solvents exhibit non-Newtonian behavior that may be analyzed by a micro rheometer. The device's small size and the requirement of only tiny amounts of sample fluid are characteristics well suited to analyzing rare proteins. Potential medical applications include the analysis of blood, through a hand-held device capable of assessing the risk of different blood-related conditions.

In Sect. 2, we present the Carreau viscosity model, and analyze its viscous behavior at different rates of shear for different parameter values. The electrokinetic flow equations are described, along with their appropriate boundary conditions. We introduce the statistical measures used to recover quantitative information from the end wall pressure profile, and describe the numerical methods employed to discretize and solve the flow problem.

In Sect. 3, flow solutions are presented and the flow profiles discussed. The simulated behavior of the dynamic viscosity is then analyzed in order to choose a range of model parameters over which the end wall pressure profile is sensitive.

In Sect. 4, we introduce the inverse problem. A new method to test for mapping uniqueness based on numerical polygonal interpolation is described, and applied to the T-junction data to demonstrate a one-to-one mapping between the Carreau fluid properties  $\lambda$  and  $n$  and the end wall pressure. We also describe a method for finding the inverse solution, based on local direct search error minimization.

In Sect. 5, we discuss the challenges that must be overcome in order for a practical micro-rheometer to be constructed. A range for pressure sensitivity is calculated, and the limitations of the work are discussed.

---

## 2 Model

### 2.1 Carreau viscosity

For Newtonian fluids, the relationship between the stress tensor and the rate of deformation tensor is a simple scalar. This scalar uniquely defines a constant viscosity  $\mu$ . For some complex fluids, the deformation tensor in a unidirectional flow can be characterized by a single parameter—the shear rate  $\dot{\gamma}$ . The simplest non-Newtonian behavior of a fluid is (Schowalter 1978; Bird et al. 1960; Doi and Edwards 1995)

$$\mu = \mu(\dot{\gamma}).$$

More generally, this relationship is tensorial, and can even depend on the deformation history of a fluid element. In this study, we use a four-parameter Carreau viscosity model, which has widespread use in the literature. The fluid viscosity at any position is dependent on

the local instantaneous shear rate  $\dot{\gamma}$ . The Carreau viscosity is given by

$$\mu = \mu_\infty + (\mu_0 - \mu_\infty) \left[ 1 + (\lambda \dot{\gamma})^2 \right]^{\frac{n-1}{2}} \tag{1}$$

The model parameters  $\mu_0$ ,  $\mu_\infty$ ,  $\lambda$  and  $n$  are the viscosity at zero shear rate, viscosity at infinite shear rate, time shear relaxation constant and exponential index, respectively. The time shear relaxation  $\lambda$  has units of seconds, and may take values in the range  $0 < \lambda < \infty$ . The exponential index  $n$  is dimensionless and takes values in the range  $0 < n < 1$ .

The parameters  $\mu_0$  and  $\mu_\infty$  are upper and lower limits for the value of viscosity, while  $\lambda$  and  $n$  determine the behavior of the viscosity curve as shear rates change. It is therefore proposed that a viscometric flow will be sensitive to the shape of the viscosity curve determined by  $\lambda$  and  $n$ . The viscosity limits  $\mu_0$  and  $\mu_\infty$  serve to scale the value of viscosity, but do not affect the dynamic behavior of the viscosity curve as shear rates change. Figure 1 shows three examples of Carreau viscous responses to shearing. Figure 1a (top) shows rapid shear response, dimensionless  $\lambda^* = 0.01$ , for which the viscosity profile is practically Newtonian. Figure 1c (top) shows the opposite extreme of a slow response time,  $\lambda^* = 20$ , for which only low shear rates induce a significant non-Newtonian character. The intermediate case, Fig. 1b (top) is responsive over a wide range of shearing. For fixed  $n$ , these curves collapse when  $\mu$  is

plotted against  $\lambda \dot{\gamma}$ . In this study, we assume that  $\mu_0$  and  $\mu_\infty$  are known, and we vary  $\lambda$  and  $n$  independently.

For a given electrokinetic driving force, there is a maximum shear rate  $\dot{\gamma}_{max}$  such that the shear rate experienced by the fluid at any point in the domain lies in the range

$$0 \leq \dot{\gamma} \leq \dot{\gamma}_{max} \tag{2}$$

We wish to choose flow conditions so that the resultant flow profile is sensitive to the Carreau parameters  $\lambda$  and  $n$ . Analysis of the Carreau viscosity curve over a range of  $\lambda$  and  $n$  values suggests that there are upper and lower limits for the values  $\lambda$  and  $n$  beyond which the viscosity curve becomes insensitive to changes in the Carreau parameters. These limits are dependent solely on the maximum shear rate experienced in the channel.

If the viscosity curve is not sensitive to different fluid parameters, then the flow profile will also be insensitive. We consider the behavior of the viscosity curve over a wide range of  $\lambda$  and  $n$  values, and choose appropriate ranges for each parameter over which the viscous response of the fluid remains sensitive to the shear rate.

As  $\lambda \rightarrow 0$ , the term  $\left[ 1 + (\lambda \dot{\gamma})^2 \right]$  in Eq. 1 tends to unity, and the viscosity becomes constant. We must therefore choose a lower bound for  $\lambda$  such that the viscosity remains “sensitive enough” over the range of shear rates present in the T-junction. Similarly, as  $n \rightarrow 1$ , viscosity also becomes constant, so an appropriate

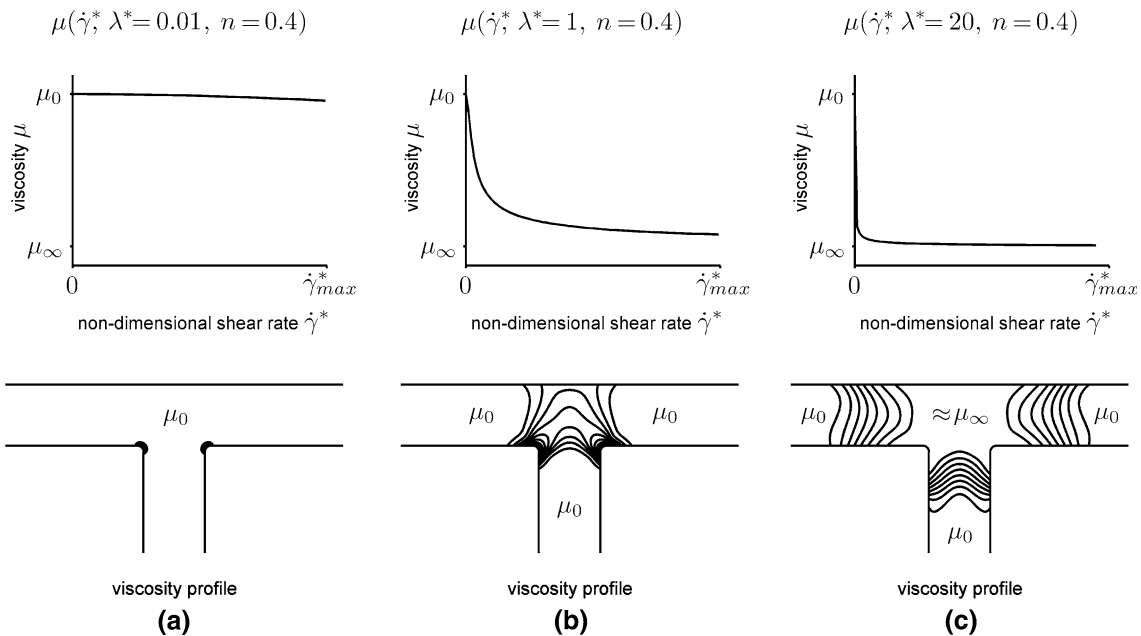


**Fig. 1** Carreau viscosity functions versus shear rate for different values of  $\lambda^*$ . Part **a** shows a typical viscosity response to shear and viscosity distribution in the T-junction when  $\lambda^*$  is small compared to  $\dot{\gamma}_{max}^*$ . Shear thinning is insignificant over the shear range and therefore the flow profile is near-Newtonian in character. Part **b** shows the same information but for the case when the viscosity

response varies across the whole shear range. The resultant flow profile is sensitive to changes in  $\lambda^*$  and  $n$  as viscous information is propagated throughout the flow. For  $\lambda^*$  of the order of  $\dot{\gamma}_{max}^*$ , as shown in **c**, shear thinning occurs at low shear. This renders the viscosity near-constant in the center of the flow where the majority of shearing takes place

upper bound for  $n$  must be chosen to ensure sensitivity. These cases correspond to curve a in Fig. 1.

When  $\dot{\gamma}_{\max} \gg 1/\lambda$ , the  $(\lambda\dot{\gamma})^2$  term in Eq. 1 becomes large, so that the Carreau viscosity approaches  $\mu_\infty$  at shear rates much smaller than  $\dot{\gamma}_{\max}$ , and is therefore near-constant over much of the shear rate range (curve c in Fig. 1). This places a restriction on the upper bound for  $\lambda$  for the viscosity to remain sensitive.

We determine appropriate ranges for  $\lambda$  and  $n$  for a fixed  $\dot{\gamma}_{\max}$ , which is dependent on the applied electrokinetic driving force. Variation of the electric field strength would change the ranges of  $\lambda$  and  $n$  over which the flow is sensitive. The choice of parameter ranges is discussed in Sect. 2.

## 2.2 Equations

Governing equations for electrokinetic flow that include species transport, temperature and electrical property variation are derived in Ermakov et al. (1998) and MacInnes (2002). The electrical double layer is not resolved directly, but instead replaced by a slip boundary condition for velocity that gives equivalent boundary conditions for the core flow. This condition is derived using a local one-dimensional solution to the Poisson–Boltzmann equation, and the validity criterion for this approximation (MacInnes 2002) is  $\kappa^2 L_0^2 \gg \max[1, (E_0 L_0/\zeta_0)^2]$ , where  $L_0$  is the channel width,  $E_0$  the electric field strength and  $\zeta_0$  is the wall zeta potential.  $\kappa$  is the inverse of the Debye length, which is the characteristic thickness of the double layer. We consider a channel of width 200  $\mu\text{m}$  in this study. With a Debye length of less than 10 nm and channel sizes of the order of 100  $\mu\text{m}$ , the layer model approximation is excellent for the flow regimes considered here (MacInnes 2002).

We assume that there is no net charge on the fluid, that the flow is in a steady state, and that the wall zeta potential and electrical conductivity of the fluid are uniform. Thermostatic conditions are assumed to apply, although dimensional analysis (MacInnes 2002) suggests that temperature variation may be significant in the region of the T-junction corners. We leave analysis of heat generation and its potential effect on the flow to future work. The equations reduce to a set of three partial differential equations for the conservation of mass, momentum and electrical charge.

The equations are solved in non-dimensional form using the reference scales  $\rho$ ,  $\mu_0$ ,  $U_0$ ,  $L_0$  and  $E_0$  for density, viscosity, velocity, length and electric field, respectively. Density is taken as constant, we use the Carreau zero-shear viscosity  $\mu_0$  as our reference viscosity, and the length scale is set according to the channel width. The non-dimensional variables are

$$x_i^* = \frac{x_i}{L_0}, \quad u_i^* = \frac{u_i}{U_0}, \quad p^* = \frac{pL_0}{\mu_0 U_0}, \quad \phi^* = \frac{\phi}{E_0 L_0}, \quad (3)$$

where  $x_i^*$ ,  $u_i^*$ ,  $p^*$ , and  $\phi^*$  are the non-dimensional length, velocity, pressure and electric potential, respectively.

The velocity scale is set according to the *Helmholtz–Smoluchowski* slip boundary condition, so that

$$U_0 = \frac{\varepsilon \zeta_0 E_0}{\mu_s}, \quad (4)$$

where  $\varepsilon$  is the electrical permittivity of the fluid,  $\zeta_0$  is the electric zeta potential at the channel wall and  $\mu_s$  is the solvent viscosity. Since the Debye length of the electric double layer is less than 10 nm, inside such a thin region one can hardly find any polymer molecules due to the depletion effect (Tuinier and Taniguchi 2005). Thus, the solvent viscosity is the appropriate viscosity for determination of the boundary slip velocity, Eq. 4. In practice, the electric field strength  $E_0$  is set to achieve the desired slip velocity, and therefore the maximum shear rate in the channel  $\dot{\gamma}_{\max}$ .

The fluid velocity is governed by the Navier Stokes momentum equations

$$Re u_j^* \frac{\partial u_i^*}{\partial x_j^*} = -\frac{\partial p^*}{\partial x_i^*} + \frac{\partial}{\partial x_j^*} \left[ \mu^* \frac{\partial u_i^*}{\partial x_j^*} \right] \quad (5)$$

and the continuity equation

$$\frac{\partial u_j^*}{\partial x_j^*} = 0, \quad (6)$$

where the Reynolds number is calculated according to the zero shear viscosity  $\mu_0$ :

$$Re = \frac{\rho U_0 L_0}{\mu_0}. \quad (7)$$

Electric charge conservation, in the case of uniform permittivity and in the absence of net charge reduces to

$$\frac{\partial}{\partial x_j^*} \left( \frac{\partial \phi^*}{\partial x_j^*} \right) = 0, \quad (8)$$

so that the electric field is independent of the velocity field.

The Carreau model parameters  $\mu_\infty$  and  $\lambda$  are normalized as

$$\mu_\infty^* = \frac{\mu_\infty}{\mu_0}, \quad \lambda^* = \frac{\lambda U_0}{L_0}, \quad (9)$$

while the exponential index  $n$  is already a non-dimensional parameter. The Carreau viscosity may then be expressed in non-dimensional form as

$$\mu^* = \mu_\infty^* + (1 - \mu_\infty^*) \left[ 1 + (\lambda^* \dot{\gamma}^*)^2 \right]^{\frac{n-1}{2}}. \quad (10)$$

The non-dimensional shear rate  $\dot{\gamma}^*$  is computed from the velocity field and is given by

$$\dot{\gamma}^* = \sqrt{2 \left( \frac{\partial u_1^*}{\partial x_1^*} \right)^2 + \left( \frac{\partial u_1^*}{\partial x_2^*} + \frac{\partial u_2^*}{\partial x_1^*} \right)^2 + 2 \left( \frac{\partial u_2^*}{\partial x_2^*} \right)^2}. \quad (11)$$

The flow is governed by the four dimensionless parameters  $Re$ ,  $\mu_\infty^*$ ,  $\lambda^*$  and  $n$ . For this computational

study, we assume a Reynolds number of  $Re = 0.02$ , which is consistent with observed experimental electrokinetic micro flows (MacInnes et al. 2003a, b) and fix the infinite shear viscosity as equal to  $\mu_{\infty}^* = 0.001$ . This is approximately the highest value given in Table 1.

### 2.3 Boundary conditions

In non-dimensional form, the boundary conditions at the channel walls are the electrokinetic slip velocity and zero electric flux through the wall:

$$u_i^* = \frac{\partial \phi^*}{\partial x_j^*}, \quad n_j \frac{\partial \phi^*}{\partial x_j^*} = 0. \quad (12)$$

$n_j$  is the local unit vector normal to the channel wall. The flow is purely electrokinetic; no external pressure gradient is applied. We therefore set the pressure at the inlet and outlets to zero. The electric potential is set to zero at the outlets. At the inlet, we set the value of  $\phi^*$  so as to produce a potential gradient in the inlet channel of unity:

$$\text{Inlet : } p^* = 0 \quad \phi^* = 8,$$

$$\text{Outlets : } p^* = 0 \quad \phi^* = 0.$$

In a straight channel section, in order to produce a potential gradient of unity in the channel,  $\phi^*$  at the inlet should be set equal to the non-dimensional channel length.

The value of  $\phi^*$  at the inlet effectively sets  $\varepsilon \zeta_0$  and thus the Reynolds number through the wall slip velocity  $U_0$ . The applied potential at the channel inlet is a physically adjustable operating parameter, which is often used in experimental work to achieve a desired slip velocity, since  $\zeta_0$  is not known *a priori* for many mixtures of macromolecules.

### 2.4 Statistical pressure analysis

We wish to extract quantitative information from the shape of the end wall pressure profile. We do so by computing the first three statistical moments of pressure

on the end wall—the mean  $\overline{p^*}$ , standard deviation  $\sigma$  and skewness  $S$ . The T-junction domain has a line of symmetry down its center, so the pressure profile will be symmetrical about the channel center. Skewness is a measure of the asymmetry of a distribution, so in order for the skewness to yield meaningful information, we consider only one half of the entire end wall pressure profile.

Standard deviation and skewness are computed from the expansions

$$\sigma = \sqrt{\overline{p^{*2}} - \overline{p^*}^2}, \quad (13)$$

$$S = \frac{1}{\sigma^3} (\overline{p^{*3}} - 3\overline{p^*}\overline{p^{*2}} + 2\overline{p^*}^3). \quad (14)$$

The  $\overline{p^{*N}}$  are obtained by integrating  $p^{*N}$  along the left half of the end wall boundary (line  $AB$  in Fig. 2) and normalizing:

$$\overline{p^{*N}} = \frac{1}{a} \int_{AB} p^{*N} dx, \quad (15)$$

where  $a$  in the above equation represents the length of the line  $AB$ .

### 2.5 Numerical methods

The model equations are discretized using the Galerkin finite element method. We use Lagrange cubic elements for the velocities  $u_i^*$  and electric potential  $\phi^*$ , and Lagrange quadratic elements for the pressure  $p^*$ . The coupling of velocity to electric field through the wall boundary conditions necessitated the use of additional weak boundary constraint equations, which were discretized using Lagrange quadratic elements. The full system of equations was solved using an iterative quasi-Newton solver with a convergence criterion of  $O(10^{-6})$  for the squared error residuals. Computations were carried out using the FEMLAB® (version 2.3 Comsol, Stockholm) finite element PDE engine on a Linux workstation, using a custom-built MATLAB® program.

Figure 2 shows the microchannel domain and a typical mesh. A 12,330-element mesh was used for the computations, with elements concentrated at the chan-

**Table 1** Representative values for Carreau parameters  $\lambda$  and  $n$

Fluid	$\mu_0$ (Pa s)	$\mu_{\infty}$ (Pa s)	$\lambda$ (s)	$n$	$\mu_{\infty}^*$	$\lambda^{*a}$
2% Polyisobutylene in Primol 355	923	0.15	191	0.358	$1.63 \times 10^{-4}$	3,820
0.75% Separan-30 in 95/5 mixture by weight of water–glycerol	10.6	0.010	8.04	0.364	$9.43 \times 10^{-4}$	160.8
7% A1 soap in decalin and m-cresol	89.6	0.010	1.41	0.200	$1.11 \times 10^{-4}$	28.2
5% Polystyrene in Aroclor 1242	101	0.059	0.84	0.380	$5.84 \times 10^{-4}$	16.8
Linear Polystyrene in 1-chloronaphthalene solution <sup>b</sup>	166	0.01	0.017	0.538	$6.02 \times 10^{-5}$	0.34

Data taken from Tanner (2002)

<sup>a</sup>Values for  $\lambda^*$  are calculated according to the density of water,  $\rho = 10^3 \text{ kg m}^{-3}$

<sup>b</sup>Taken from Zimmerman (2004)

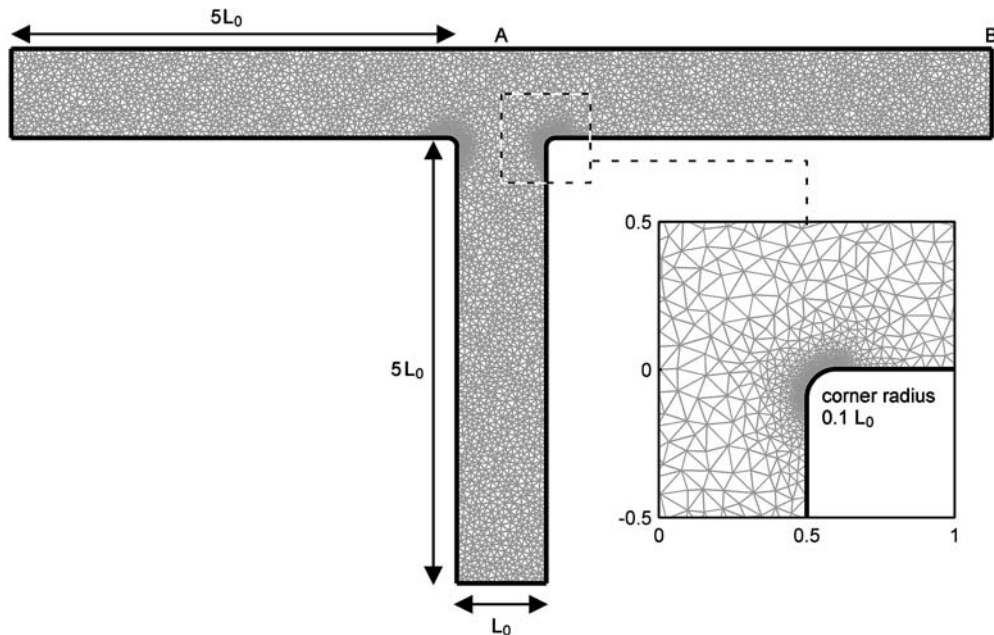


**Fig. 2** Two-dimensional microchannel domain. The inlet and outlet arms of the T-junction are five channel widths long to ensure that flow is developed at the inlet and outlet boundaries. The finite element mesh consists of 12,330 triangular elements; mesh

nel corners where the largest flow gradients occur, and mesh accuracy was verified on a refined 19,782-element mesh. When modeling a flow domain with sharp corners, a large number of elements are required in the corner regions in order to resolve the large flow gradients (see inset diagram in Fig. 2). It is demonstrable that the mesh size in these corner regions determines the upper limit for the calculated flow gradients. Large flow gradients may introduce terms in the solution vector of several orders of magnitude higher than other terms, leading to impaired convergence. In practice, the perfect T-junction does not exist as wet etching microchannel fabrication processes smooth sharp edges. MacInnes 2002 actually found closer agreement between numerical simulations and experiments when rounded corners were modeled. We found that curvatures smaller than a given level were found to make negligible difference to the back wall pressure profile. In light of these considerations, we rounded the corners with a radius of one tenth of the channel width. The error introduced by this approximation was found to influence the flow locally over a length scale of the order of the radius of curvature and had a negligible effect on the flow as a whole.

### 3 Forward problem

#### 3.1 Typical flow profile

A computed steady-state flow profile with  $\lambda^* = 1$  and  $n = 0.6$  is shown in Fig. 3. The plug velocity profile in the inlet channel is characteristic of pure electroosmotic flow, and has the advantage for non-Newtonian fluids

resolution is higher at the channel corners where larger flow gradients occur. Boundary integration of the pressure  $p^*$  is performed along the line  $AB$ . The finite element approximation solves for 197,965 unknowns

that the shear rate is zero, so that viscosity remains uniform.

As the fluid approaches the junction, large shear rates are experienced close to the walls as the fluid is “dragged” around the corners through the slip boundary conditions. Velocity vectors are seen to be several times larger in magnitude at the corners than in the channel flow, owing to the large potential gradients there (Patanekar and Hu 1998). The flow is forced to diverge, and a range of shear rates are present in the vicinity of the corners. The centerline velocity of the fluid is forced to zero at the end wall, where a stagnation point is clearly visible.

A range of shear rates is also present along the end wall, as the potential gradient becomes larger in magnitude approaching the outlets. Shear rates in this region are an order of magnitude smaller than the shear rates near the corners, and within two channel widths of the junction the flow regains a near-plug profile. Therefore it is the high shear rates at the corners that produce a viscometric flow, while the shear rates near the stagnation point are small in comparison. The presence of small shear rates along the back wall suggests that the flow could be “squeezed” into a narrower back channel to produce larger shear rates over the whole of the end wall and increase sensitivity to the Carreau parameters.

#### 3.2 Choice of parameter ranges

Our simulations show that the flow profile is sensitive to variation of the Carreau viscosity parameters  $\lambda^*$  and  $n$ . We chose the shape of the pressure profile on the end

wall of the channel as a measure of changes to the flow field. Figure 3 demonstrates the velocity vectors and pressure profile for a typical set of Carreau parameters. The bottom of Fig. 1 shows the viscosity variation induced by the velocity field. Significant variation in viscosity profile and pressure shape is apparent as the Carreau parameters are changed. We wish to choose appropriate ranges for  $\lambda^*$  and  $n$  over which such variations remain pronounced. These ranges are selected by considering the shape of the viscosity curve as described in Sect. 1, together with simulated flow profiles.

Contours of dynamic viscosity and a plot of end wall pressure corresponding to  $\lambda^* = 1, n = 0.5$  are shown in Fig. 4a. The largest changes in viscosity occur in the vicinity of the corners where shear rates are large, while the viscosity changes little in the central region of the junction near to the end wall.

The pressure plots show the expected symmetry about the channel center. The ‘‘Mexican’’ hat shape of the back wall pressure profile recurs at all parameters studied, including purely Newtonian flow. Notice that the pressure is lower than the reference pressure  $p^* = 0$  everywhere on the end wall apart from near the center line. This pressure drop is due to the influence of the velocity slip boundary conditions at the corners, which drag the fluid away from the end wall. The rise along the end wall away from the central maximum is due to the acceleration up to the free stream velocity from the stagnation point. The small deviation from zero pressure at the exit is a numerical artifact of requiring the boundary condition to be fully developed flow (uniform pressure outflow). It is clear that both the position and shape of the central maximum changes with  $\lambda^*$  and  $n$ , implying that mean and standard deviation are suitable measures with which to analyze the pressure profile.

The case when  $\lambda^* = 0.4$  and  $n = 0.2$  is shown in Fig. 4b. The viscosity variation is seen to be confined to an area near the corners, where the shear rates are

largest. The viscosity approaches the infinite shear viscosity at higher shear rates than in case (a), meaning that it is insensitive to the smaller shear rates that are present further from the channel corners. This flow demonstrates the approach to the limiting case where  $\lambda \rightarrow 0$ , as discussed in Sect. 1.

In order to ensure sensitivity for the range of shear rates present in the T-junction flow, the normalized Carreau parameters are varied independently over the following ranges:

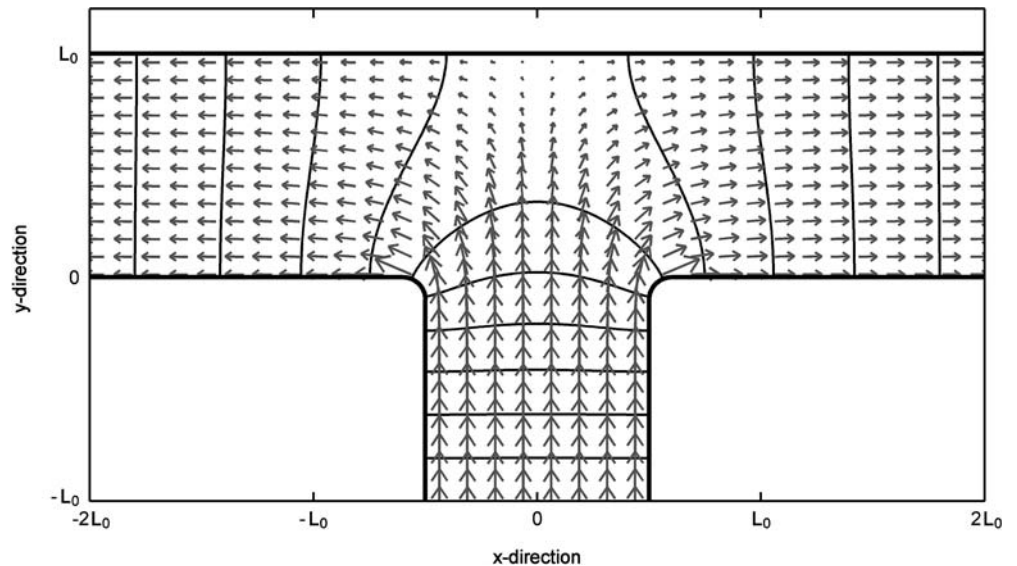
$$0.3 \leq \lambda^* \leq 10, \quad (16)$$

$$0.35 \leq n \leq 0.9. \quad (17)$$

We may consider our model as a function  $\mathbf{f}$  that maps a vector of input parameters  $\mathbf{x}_i = (\lambda_i^*, n_i)^T$  to a vector of outputs,  $\mathbf{y}_i = (\bar{p}_i^*, \sigma_i, S_i)^T$ . Our output vectors  $\mathbf{y}_i$  lie in the set  $\mathbf{Y} \subset \mathbb{R}^3$ , where  $\mathbf{Y} = \mathbf{f}(\mathbf{X})$ . The set  $\mathbf{Y}$  of all output vectors is the image of the set  $\mathbf{X}$  of all input vectors with respect to the model  $\mathbf{f}$ . Specifically,  $\mathbf{Y}$  represents a two-dimensional surface in  $\mathbb{R}^3$ , parameterized by the two input parameters  $\lambda^*$  and  $n$ .

In the upper and lower limits for  $\lambda^*$ , the viscosity becomes insensitive to shear rate, and the flow profile becomes close to that of a Newtonian fluid with constant viscosity. The parameter ranges are set so that the flow profiles at  $\lambda^* = 0.3$  and 10 remain distinct to some tolerance, which could be set according to experimental error for example. Similarly, when  $n \rightarrow 1$ , viscosity becomes constant;  $n = 0.9$  was chosen as the upper limit at which the flow profile is distinct from that of Newtonian flow. This range is approximately the parametric range for which the numerical map of Fig. 6 from parameters  $(\lambda^*, n)$  to measures  $(\bar{p}^*, \sigma, S)$  are single valued. In this range an online sensor would invert the measures to find the constitutive parameters  $\lambda$  and  $n$ . For values of  $\lambda^*$  that are higher or lower, the procedure becomes numerically insensitive. This can be addressed with higher resolu-

**Fig. 3** Velocity vectors and contours of electric potential for the case when  $\lambda^* = 1$  and  $n = 0.6$ . Velocities are larger at the corners owing to the large potential gradients there. The maximum shear rate  $\dot{\gamma}_{\max}$  always occurs at the channel corners. Its value is governed not only by the slip velocity, but also by the values of the Carreau parameters  $\lambda$  and  $n$



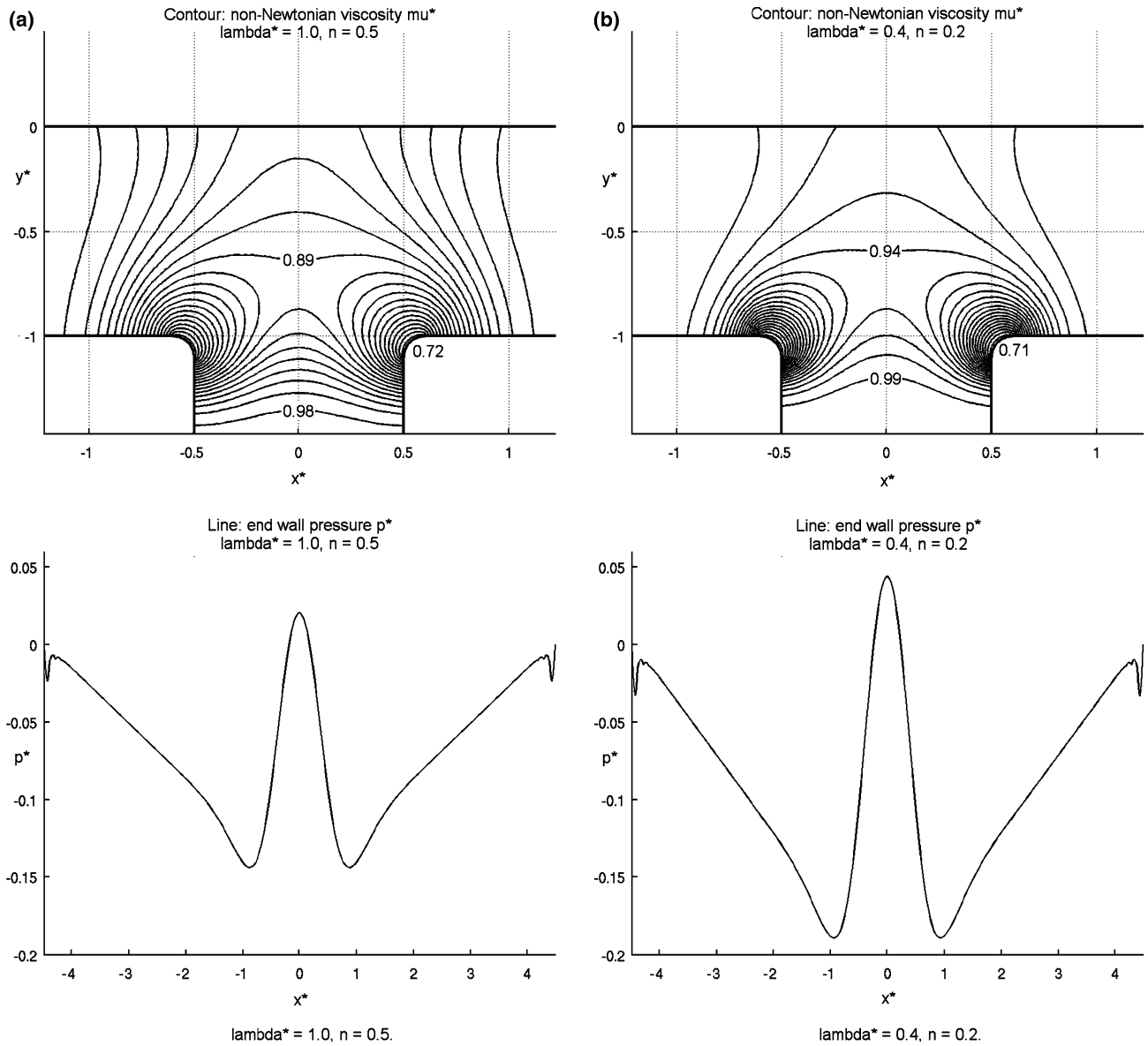


**Fig. 4** Contours of dynamic viscosity  $\mu^*$  and plots of end wall pressure  $p^*$  for two pairs of Carreau parameters. The flow profile is seen to be sensitive to changes in the constitutive properties  $\lambda^*$  and

$n$ . The height and width of the pressure maximum is seen to vary, implying that statistical analysis of the end wall pressure should be informative

tion PDE solution to some extent, but there will always be a numerically insensitive limit in  $\lambda^*$  at fixed resolution. At low  $n$ , the mapped image set  $\mathbf{Y}$  curls back on itself and becomes double valued. Because  $\lambda^*$  is a dimensionless operating parameter, it can be adjusted experimentally by changing the electric field strength to move to a numerically sensitive region.  $n$ , however, is a physical parameter which is intrinsically double valued in the near zero region due to change in shape of the Carreau viscosity profile.

Variation of the channel size  $L_0$  and the slip velocity  $U_0$  through the inlet potential allows the maximum shear rate in the channel  $\dot{\gamma}_{\max}$  to be altered. This should allow the classification of fluids over large ranges of  $\lambda$ . The

sensitivity ranges apply to the normalized  $\lambda^*$ , where  $\lambda^* = \lambda U_0/L_0$ , so by changing our variable scalings, it is possible to consider fluids with high  $\lambda$  by reducing the slip velocity  $U_0$ , while fluids with small  $\lambda$  could be analyzed by reducing the channel width  $L_0$ .

#### 4 Inverse problem

Next we address the question of invertibility—given experimental pressure measurements, can we infer the viscous properties of an unknown fluid? For inversion to be possible, we need to show the existence of a one-to-one mapping between the parameters that we intend to



vary,  $\lambda^*$  and  $n$ , and the quantities that we intend to measure, namely  $\bar{p}^*$ ,  $\sigma$  and  $S$ .

4.1 Numerical test for solvability of the inverse problem

A necessary and sufficient condition for the inverse problem to be unique is that the surface  $\mathbf{Y} \subset \mathbb{R}^3$  does not intersect itself. In other words, every input  $\mathbf{x}_i \in \mathbf{X}$  is mapped by  $\mathbf{f}$  to a unique output  $\mathbf{y}_i \in \mathbf{Y}$ . For a surface not to touch itself, the inverse function theorem states that  $\det J$ , where  $J_{ij} = (\partial f_i / \partial x_j)$  is the Jacobian of the map  $y = f(x)$ . Where  $\det J = 0$  the surface must touch itself, which is equivalent to stating that two or more mapped image points intersect there, and hence the map is not invertible. In the case, as here, that the Jacobian of the map is not a square matrix, then this condition applies the rank of the largest square submatrix being equal to its dimension.

A technique based on linear triangular polygonal interpolation is used to determine whether the mapping  $\mathbf{f} : \mathbf{X} \rightarrow \mathbf{Y}$  is single-valued. We approximate the continuous set  $\mathbf{X}$  by defining interpolation functions between each discrete data point, as shown schematically in Fig. 5. Firstly, step sizes  $\delta \mathbf{x} = (\delta \lambda^*, \delta n)^T$  are chosen between the data points  $\mathbf{x}_i$  to be evaluated. We then have  $m$  data points. Triangular polygons are defined according to the data points at their vertices, with two polygons interpolating each two-dimensional interval  $\delta \mathbf{x}$ . For example, the interval between the data points  $\mathbf{x}_1, \mathbf{x}_2, \mathbf{x}_3$  and  $\mathbf{x}_4$  in Fig. 5 is interpolated by polygons  $P_1$  and  $P_2$ , where  $P_1 = (1, 2, 5)$  and  $P_2 = (2, 6, 5)$ .

The  $m$  output points  $\mathbf{y}_i$  are computed by running the model with each set of input parameters  $\mathbf{x}_i$ . This batch process is entirely automated from within MATLAB®. A discrete set of points  $\mathbf{y}_i \in \mathbf{Y}$  is obtained, from which the approximate continuous surface  $\mathbf{Y}$  may be constructed

by drawing the polygons  $P_1, P_2, \dots, P_m$  in  $\mathbb{R}^3$  with their vertices at the output points  $\mathbf{y}_1, \mathbf{y}_2, \dots, \mathbf{y}_m$ . The resulting surface intersects itself if and only if at least one pair of polygons overlap. The interpolated set  $\mathbf{Y}$  may be displayed graphically to examine for overlapping polygons, or it can be analyzed numerically to search for intersections. Software with this capability is freely available, for example the open source *GNU Triangulated Surface Library* (website: <http://www.gts.sourceforge.net>).

4.2 Graphical analysis

We perform a graphical analysis of the mapping  $\mathbf{f} : \mathbf{X} \rightarrow \mathbf{Y}$ . Pictures of the interpolated sets  $\mathbf{X}$  and  $\mathbf{Y}$  are shown in Fig. 6. The input parameter set  $\mathbf{X} \in \mathbb{R}^2$  is shown in Fig. 6a, and the lower and upper bounds for  $\lambda^*$  and  $n$  are marked as points  $A, B, C$  and  $D$ . A chequered pattern is drawn on the surface to emphasize the scaling that occurs when the input set is mapped to the output. The picture represents the entire range of values of  $\lambda^*$  and  $n$  that our model parameters may take. In this study, we take  $\delta \lambda^* = 0.1$  and  $\delta n = 0.05$ , so that 1,700 data points are computed in order to construct the interpolated sets. Computations took one week to complete on a Linux workstation.

The interpolated output set  $\mathbf{Y}$  is pictured in Fig. 6b. The set  $\mathbf{X}$  has been distorted considerably, with straight edges becoming curved and elongated, but it is clear from the figure that  $\mathbf{Y}$  does not intersect itself and is a smooth surface. The bounds at  $A-D$  are shown for direct comparison with the input parameter set. Point  $D$  represents the point of minimum  $\lambda^*$  and  $n$ , and the directions of increasing Carreau parameter values are drawn on the surface at this point.

We may analyze parameter sensitivity (Sun et al. 2001; Chen et al. 2004) by examining how the size of the chequered pattern varies at different points on the output surface. Looking at Fig. 6a,  $\lambda^*$  varies from 0.3 at edge  $AD$  of  $\mathbf{X}$  to 10 at edge  $BC$  of  $\mathbf{X}$ , with constant step size  $\delta \lambda^* = 0.1$ . We see from Fig. 6b that in output space, the distance between each successive  $\mathbf{x}_i$  decreases as  $\lambda^*$  increases. The pressure profile is less sensitive to changes in the Carreau shear relaxation time parameter as that parameter increases. We also see that the pressure profile is least sensitive to changes in  $n$  at low values of  $n$ , by comparing polygon sizes at edges  $AB$  and  $CD$ .

Generation of the interpolated mapping supplies us with all of the information needed to examine the sensitivity of the statistical moments  $\bar{p}^*, \sigma$  and  $S$  individually, although such an analysis has not been carried out in this study.

In summary, it is clear that the inverse problem is uniquely solvable in a broad range of the Carreau fluid parameters  $\lambda^*$  and  $n$  and the first three statistical moments of the end wall pressure,  $\bar{p}^*, \sigma$  and  $S$ . The pressure is less sensitive to the fluid properties as the time shear relaxation parameter  $\lambda^*$  increases. The extent to which we may accurately distinguish between two different sets

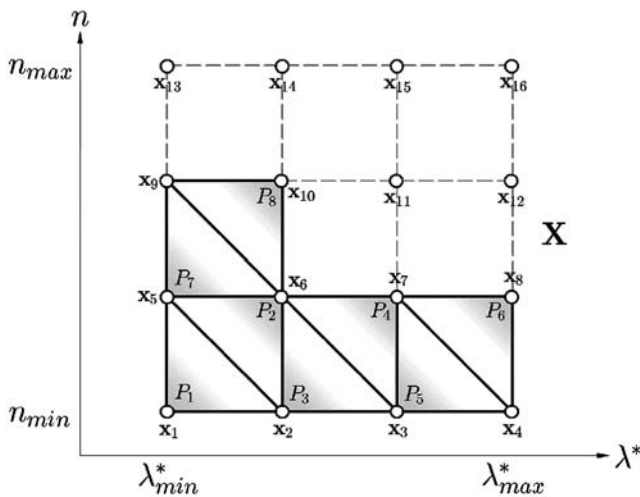
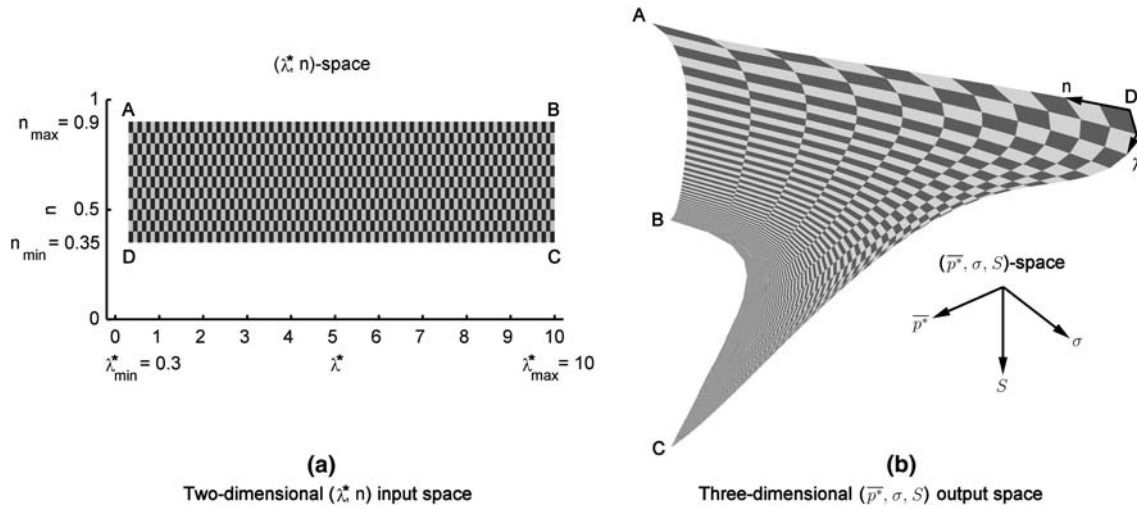


Fig. 5 Triangular polygons are used to linearly interpolate the discrete data points  $\mathbf{x}_i$ . The continuous sets  $\mathbf{X}$  and  $\mathbf{Y}$  may then be approximated



**Fig. 6** The interpolated sets  $\mathbf{X}$  and  $\mathbf{Y}$  are shown graphically. The range over which  $\lambda^*$  and  $n$  are varied is shown in **a**. The chequered pattern indicates the step sizes  $\delta\lambda^* = 0.1$  and  $\delta n = 0.05$  used in computations. The set  $\mathbf{X}$  of  $(\lambda^*, n)$ -points in  $(\lambda^*, n)$ -space is mapped to the set  $\mathbf{Y}$  of  $(\lambda^*, n)$ -points in  $(\bar{p}^*, \sigma, S)$ -space, shown in **b**. It is

clear that the set  $\mathbf{Y}$  does not intersect itself in  $(\bar{p}^*, \sigma, S)$ -space. Thus the inverse problem is well posed, and we may determine the Carreau properties  $\lambda^*$  and  $n$  from a single  $(\bar{p}^*, \sigma, S)$ -measurement. The pressure profile is seen to become less sensitive to changes in the Carreau parameters as  $\lambda^*$  increases and  $n$  decreases

of potential fluid properties would be governed by our measurement error in an actual experiment. If this error proved to be large, we may wish to restrict our “micro-rheometer” to the classification of fluids with smaller  $\lambda^*$  to ensure accuracy in our predictions.

### 4.3 Solution of the inverse problem

A local search method based on an error minimization approach may be used to obtain the unique Carreau parameters (model inputs) that correspond to an observed set of pressure moments (model outputs). Recall that our model may be expressed as a function  $\mathbf{f}$ , acting on a vector of input parameters  $\mathbf{x}_i$  to produce a vector of outputs  $\mathbf{y}_i$ . Suppose that we have an output vector  $\mathbf{y}_0$ , perhaps obtained from an experiment. We wish to find the corresponding input vector  $\mathbf{x}_0$  such that  $\mathbf{f}(\mathbf{x}_0) = \mathbf{y}_0$ . An initial guess  $\mathbf{x}_k$  is chosen for the required input parameters. The corresponding output vector  $\mathbf{y}_k$  is then evaluated as  $\mathbf{y}_k = \mathbf{f}(\mathbf{y}_k)$ .

The squared error  $E_k$  between the target output vector and the output vector corresponding to the guessed input is formed as

$$E_k = (\mathbf{y}_0 - \mathbf{y}_k)^T (\mathbf{y}_0 - \mathbf{y}_k), \quad (18)$$

so that  $E_k = 0$  if and only if  $\mathbf{y}_0 = \mathbf{y}_k$ . We may then minimize  $E_k$  subject to  $\mathbf{x}_k$  to find the value of  $\mathbf{x}_0$ . When a local minimum is found, by the uniqueness of the mapping  $\mathbf{f}$ , we must have  $\mathbf{x}_k = \mathbf{x}_0$  at that minimum.

A direct search method based on the Nelder–Mead amoeba algorithm (Nelder and Mead 1965) was used to find inverse solutions from computed pressure data. This method was selected as it does not require numerical or analytic gradients, which cannot be calculated directly

for our model function  $\mathbf{f}$ , and because it was readily available as a standard command in MATLAB®. Inverse search methods based on the Newton method (Sun et al. 2001) which evaluate the finite element Jacobian at each step are often used in the literature, but in our case they were not viable owing to the boundary integration performed on the finite element solution to obtain the output parameters. This necessitated the use of a more general direct search method.

A potential disadvantage of using direct search methods is that they may require many function evaluations to converge to a solution. In this study, a single function evaluation requires the solution of the entire finite element model, so it is desirable to minimize the number of function evaluations necessary. This also emphasizes the importance of choosing an initial guess  $\mathbf{x}_0$  that is as close to the actual solution as possible. The numerical interpolation technique employed here allows such a starting value to be found with relative ease.

## 5 Discussion

Computations show that there is a wide parametric region for which a single-valued mapping between the Carreau fluid parameters  $\lambda$  and  $n$  and the first three statistical moments of the end wall pressure profile  $\bar{p}$ ,  $\sigma$  and  $S$  exists. This relationship allows an experimental fluid exhibiting Carreau non-Newtonian behavior to be uniquely determined by the measurement of the end wall pressure. If the Carreau properties of a fluid fall within the range  $0.3 L_0/U_0 \leq \lambda \leq 10 L_0/U_0$  (the range of parameter sensitivity for  $\lambda$ ), it may be classified by a single experiment. If the value of  $\lambda$  falls outside this range, the wall slip velocity  $U_0$  may be varied by altering

the electric potential at the inlet in order to achieve different ranges of sensitivity for  $\lambda$ .

In the numerical model, the shear rates at square corners increase with the grid resolution. Locally, at a square corner the shear rate is infinite as fluid elements instantaneously change direction. These infinite shear rates cannot be achieved numerically; the computed shear rates at the corners increase as grid resolution increases. As a compromise, the corners have been rounded with a radius of one tenth of the channel width. This approach has been used in similar computational studies (e.g. MacInnes et al. 2003a) and it allows the use of fewer grid elements while imposing a limit on the magnitude of shear rates at the corners. In the aforementioned work, which considered the electroosmotic flow of a Newtonian fluid, computations of velocity were found to be in agreement with experimental results to within the measurement uncertainty of 5 per cent. It therefore seems sensible to assume that the rounding of the channel corners introduces only small errors into the flow solution.

In real-life devices, fabrication techniques (for example glass etching) result in microchannels with shapes and dimensions that can deviate significantly from the ideal geometry considered in this study. It has been shown (MacInnes et al. 2003b) that typical variations in channel shape due to etching performance can affect the flow to the extent that model predictions can become inaccurate. Micro particle image velocimetry ( $\mu$ -PIV) techniques (Bown et al. 2005; Devasenathipathy et al. 2002; Stone et al. 2002) are being used to characterize the exact geometry of fabricated microchannels individually. Devices with geometries that differ from the ideal considered here may be calibrated experimentally, and a mapping built up by processing a range of Carreau fluids. The existence shown here of a unique inverse solution for the Carreau parameters guarantees that such a mapping is also unique, and allows the prediction of unknown fluid parameters without solving the inverse model.

Simulations demonstrate a characteristic variation of non-dimensionalized pressure  $p^*$  of about 0.2 (see Fig. 4). We calculate the actual pressure,  $p$ , from  $p^*$  using the following expression:

$$p = \frac{\mu_0 U_0}{L_0} p^* . \quad (19)$$

$\mu_0$ ,  $L_0$  and  $U_0$  are the characteristic viscosity, length and velocity scales respectively. For electroosmotic flow of an aqueous Carreau fluid in a micro-channel,  $\mu_0 = 10^2$  Pa s,  $L_0 = 2 \times 10^{-4}$  m and  $U_0 = 10^{-3}$  m s $^{-1}$ . Substituting these values into Eq. 19 gives

$$p_{\text{var}} = \frac{10^2 \times 10^{-3}}{2 \times 10^{-4}} \times 0.2 = 100 \text{ Pa} . \quad (20)$$

In order to accurately reconstruct the end wall pressure profiles from a number of discrete measurements, one

would assume that a sensor error of at most 1 Pa would be desirable. A sensor would also be required that had a footprint of no more than 50  $\mu\text{m}$  in order for it to fit into the channel. It has been shown<sup>1</sup> that inlet and outlet pressures in a micro-channel T-junction on a glass chip may be balanced to within 0.001 Pa, although integration of pressure transducers into the channel has not yet been attempted. It is reasonable to assume therefore that the pressure variations present in the T-junction simulations (100 Pa) are large enough to be measured experimentally.

It is proposed that the end wall pressure profile may be reconstructed from a number of discrete measurements from piezo-electric pressure transducers embedded at appropriate positions along the end wall. Use of such transducers in a 300  $\mu\text{m}$  microchannel to promote mixing has been demonstrated by Yaralioglu et al. (2004), although the successful implementation of such devices for pressure measurement requires further work. Once an approximate pressure profile was constructed from sensor measurements, the mean, standard deviation and skewness could be obtained. It is proposed that the calculation error for the values of  $\bar{p}$ ,  $\sigma$  and  $S$  will decrease as sensor accuracy and the number of pressure sensors along the end wall increase.

We have shown that the pressure profile is sensitive to the constitutive properties of a Carreau fluid. It is reasonable to assert that the velocity field as a whole will also be sensitive to  $\lambda$  and  $n$ . By forming statistical measures of the velocity field at different positions in the flow, it should be possible to find an invertible relationship between  $\lambda$  and  $n$  and the velocity field. The existence of such a mapping—a strong indication that the pressure mapping holds—could easily be tested experimentally through  $\mu$ -PIV techniques. PIV equipment is expensive however, whereas piezo-electric pressure sensors embedded in a microchannel are likely to be cheap to produce, and would not require specialist lab equipment to operate.

A selection of Carreau properties for different fluids is shown in Table 1. For this preliminary computational study, several assumptions were made. The fluid's zero shear and infinite shear viscosities  $\mu_0$  and  $\mu_\infty$  were fixed through the non-dimensional infinite shear viscosity and Reynolds numbers,  $\mu_\infty^*$  and  $Re$ , respectively. This results in a fixed electrokinetic slip velocity  $U_0$ . In order to change the range of  $\lambda$  sensitivity of the flow, we must change the value of maximum shear rate  $\dot{\gamma}_{\text{max}}$  that occurs at the channel corners. In general the maximum shear rate for any given flow is dependent on the Reynolds number, which in turn is dependent on both the zero shear viscosity  $\mu_0$  and the slip velocity  $U_0$ . On the other hand, our non-dimensional Carreau parameter  $\lambda^*$  is normalized by the length and velocity scales, and so is also dependent on  $U_0$ . Further simulations are required to examine these relationships more closely before concrete predictions can be made about the ranges achieved.

<sup>1</sup>H. C. H. Bandulasena (2005), Personal Communication.

able over which the flow is sensitive to the  $\lambda$ -value of a given fluid. It may be the case that the channel width  $L_0$  has a greater effect on the sensitivity range for  $\lambda$  than the slip velocity  $U_0$ .

## 6 Conclusions

Two-dimensional finite element simulations of the electrokinetic flow of a non-Newtonian fluid in a T-junction microchannel have been demonstrated. It has been shown that there exists a single-valued map between the viscous characteristics of the fluid and the end wall pressure profile for a range of non-dimensionalised Carreau parameters. Such a map allows the construction of a highly efficient viscometric device, in which a single experiment can determine the entire viscosity curve of a fluid with unknown Carreau parameters  $\lambda$  and  $n$  in the ranges  $0.3 L_0/U_0 \leq \lambda \leq 10 L_0/U_0$  and  $0.1 \leq n \leq 0.9$  if the viscosities at zero and infinite shear are known. By varying the channel size and electric field strength, it should be possible to determine the Carreau characteristics of a fluid over a much larger range of parameter values. A new method for determining parameter identifiability and sensitivity has been presented, and the resulting inverse problem solved. The effects of heat generation through electrical resistance and viscous dissipation have been neglected in this study, along with the effects of net charges on species and varying electrical properties. These potentially nonlinear effects may require the layer model to be extended in order to preserve simulation accuracy. In order for a T-junction viscometric device to be viable, these effects must be considered in future work.

**Acknowledgements** WZ acknowledges helpful discussions with Jordan MacInnes. He acknowledges support from EPSRC Grant Nos. GR/A01435 and GR/S83746 and thanks the Royal Academy of Engineering and Leverhulme Trust for a Senior Research Fellowship. TC would like to thank the University of Sheffield for a doctoral scholarship.

## References

- Bird RB, Stewart WE, Lightfoot EN (1960) *Transport phenomena*. Wiley, New York
- Bown MR, MacInnes JM, Allen RWK (2005) Micro-PIV simulation and measurement in complex microchannel geometries. *Meas Sci Technol* 16:619–626
- Chen BH, Bermingham S, Neumann AH, Kramer HJM, Asprey, SP (2004) On the design of optimally informative experiments for dynamic crystallization process modelling. *Ind Eng Chem Res* 43:4889–4902
- Devasenathipathy S, Santiago JG, Takehara K (2002) Particle tracking techniques for electrokinetic microchannel flows. *Anal Chem* 74:3704–3713
- Doi M, Edwards SF (1995) *The theory of polymer dynamics*. Clarendon, Oxford
- Ermakov SV, Jacobson SC, Ramsey JM (1998) Computer simulations of electrokinetic transport in microfabricated channel structures. *Anal Chem* 70:4494–4504
- MacInnes JM (2002) Computation of reacting electrokinetic flow in microchannel geometries. *Chem Eng Sci* 57:4539–4558
- MacInnes JM, Du X, Allen RWK (2003a) Prediction of electrokinetic and pressure flow in a microchannel T-junction. *Phys Fluids* 15(7):1992–2005
- MacInnes JM, Du X, Allen RWK (2003b) Dynamics of electroosmotic switching of reacting microfluidic flows. *Chem Eng Res Des* 81(A7):773–786
- Nelder JA, Mead R (1965) A simplex method for function minimization. *J Comput* 7:308–313
- Patankar NA, Hu HH (1998) Numerical simulation of electroosmotic flow. *Anal Chem* 70:1870–1881
- Pommer MS, Meinhart CD (2005) Shear-stress distributions surrounding individual adherent red cells in a microchannel measured using Micro-PIV. In: *Proceedings of the 6th international symposium on particle image velocimetry PIV'05*, Pasadena, California, USA, September 21–23, 2005
- Rees JM, Zimmerman WB (2005) Rheometry of electrokinetic flows in microchannels. In: *Microfluidics: theory, history and applications*, Springer Verlag Wien, CISM Lecture Series Vol. 466
- Schowalter WR (1978) *Mechanics of non-Newtonian fluids*. Pergamon, Oxford
- Stone SW, Meinhart CD, Wereley ST (2002) A microfluidic based nanoscope. *Exps Fluids* 33(5):613–619
- Sun N, Sun NZ, Elimelech M, Ryan JN (2001) Sensitivity analysis and parameter identifiability for colloid transport in geochemically heterogeneous porous media. *Water Resour Res* 37:209–222
- Tanner RI (2002) *Engineering rheology*. 2nd edn. Oxford University Press, Oxford
- Tuinier R, Taniguchi T (2005) Polymer depletion-induced slip near an interface. *J Phys: Condens Matter* 17:L9–L14
- Yaralioglu GG, Wygant IO, Marentis TC, Khuri-Yakub BT (2004) Ultrasonic mixing in microfluidic channels using integrated transducers. *Anal Chem* 76(13):3694–3698
- Zimmerman WB (2004) Process modelling and simulation with finite element methods, Chap. 9, *World Scientific Series A on Stability, Vibration and Control of Systems*, Singapore
- Zimmerman WB, Rees JM, Craven TJ (2004) Inverse problems in non-Newtonian electrokinetic flows in microchannels. *ESDA Manchester*, ASME Transactions, No. 2004 58438